

Three-stage binarization of color document images based on discrete wavelet transform and generative adversarial networks

Rui-Yang Ju ^a, Yu-Shian Lin ^b, Yanlin Jin ^c, Chih-Chia Chen ^b, Chun-Tse Chien ^b and Jen-Shiun Chiang ^{b,*}

^aGraduate Institute of Networking and Multimedia, National Taiwan University, No. 1, Sec. 4, Roosevelt Rd., Taipei City, 106335, Taiwan

^bDepartment of Electrical and Computer Engineering, Tamkang University, No.151, Yingzhuang Rd., Tamsui Dist., New Taipei City, 251301, Taiwan

^cDepartment of Electrical and Computer Engineering, Rice University, 6100 Main St., Houston, 77005, Texas, USA

ARTICLE INFO

Keywords:

semantic segmentation
discrete wavelet transform
document enhancement
document image binarization
handwriting text recognition
generative adversarial networks

ABSTRACT

The efficient segmentation of text information from the background in degraded color document images is an important challenge in the preservation of ancient manuscripts. The imperfect preservation of ancient manuscripts has led to various types of degradation over time, such as staining, yellowing, and ink seepage, badly affecting document image binarization results. This work proposes a three-stage method to generate binarization image results for degraded colour document images using generative adversarial networks (GANs). Stage-1 involves applying discrete wavelet transform and retaining the low-low subband images for document image enhancement. In Stage-2, the original input image is split into red, green, and blue (RGB) three single-channel images and one grayscale image, and each image is trained with independent GANs to extract color foreground information. In Stage-3, the output images of Stage-2 and the resized input images are used to train independent GANs to generate document binarization results, enabling the combination of global and local features. The experimental results show that the Avg-Score of the proposed method is 77.64, 77.95, 79.05, 76.38, 75.34, and 77.00 on the (H)-DIBCO 2011, 2013, 2014, 2016, 2017, and 2018 datasets, which achieves the state-of-the-art level. The implementation code for this work is available at <https://github.com/abcpp12383/ThreeStageBinarization>.

1. Introduction

Historical analyses of human societies primarily rely on reconstructing and analyzing preserved ancient documents. Parchment manuscripts and paintings have predominantly served as the means of preserving crucial ancient documents throughout the evolution of human society. Analyzing preserved ancient documents presents challenges due to potential forms of interference and degradation, including paper yellowing, text fading, page contamination and moisture damage.

Document image enhancement is one of the most important tasks in the reconstruction and analysis of ancient documents. It involves document image binarization to extract essential text information from the page. Elevating the image quality of deteriorated documents necessitates addressing various challenges, including text degradation and bleed-through issues, such as text degradation and bleed-through [1, 2, 3, 4]. However, traditional binarization methods cannot extract text information from the background of degraded documents effectively, often resulting in incomplete removal of shadows and noises, or loss of text information [5, 6, 7].

With the development of deep learning, neural networks have been applied to image binarization. Calvo-Zaragoza and Gallego [8] introduced a selectional auto-encoder approach, parsing the text through the trained network model, and performing binarization using threshold. Fully convolutional network (FCN) [9] enables the generated images to maintain the same size as the input images, and the task [10] of generating document binarization using FCN is also included in the semantic segmentation task. However, most image binarization methods primarily process grayscale documents, targeting contaminated black and white scanned ancient documents as their default.

Considering that the images of some ancient documents are in colour, we propose a novel three-stage method for document image enhancement and colour degradation document binarization. The proposed method consists of three stages. In Stage-1, we split the original input image into red, green, and blue (RGB) three single-channel images and one grayscale image, and apply discrete wavelet transform (DWT) to retain the low-low (LL) subband images and normalize them to achieve image enhancement. In Stage-2, we train four independent adversarial networks with the four single-channel images to eliminate background information and extract color foreground details from the local image patches. During the processing of Stage-3, the multiscale adversarial networks produce 224×224 image patch (local) prediction outputs and 512×512 resized image (global) prediction outputs for the document images, which are subsequently fused to obtain the final output.

To evaluate the performance of the proposed method for degraded document image binarization, we compare it with

*Corresponding author: jksen.chiang@gmail.com

jryjry1094791442@gmail.com (Rui-Yang Ju); abcpp12383@gmail.com (Yu-Shian Lin); neil.yl.jin@gmail.com (Yanlin Jin); crystal88irene@gmail.com (Chih-Chia Chen); popper0927@hotmail.com (Chun-Tse Chien); jksen.chiang@gmail.com (Jen-Shiun Chiang)

ORCID(s): 0000-0003-2240-1377 (Rui-Yang Ju); 0000-0001-9825-9958 (Yu-Shian Lin); 0000-0001-8466-0660 (Yanlin Jin); 0000-0003-0848-9747 (Chih-Chia Chen); 0009-0008-7549-4021 (Chun-Tse Chien); 0000-0001-7536-8967 (Jen-Shiun Chiang)

other methods using DIBCO datasets of 2011, 2013, 2014, 2016, 2017, and 2018 [11, 12, 13, 14, 15, 16].

The main contributions of this paper are as follows:

- Introducing a novel three-stage generative adversarial networks method for enhancing and binarizing the degraded color documents.
- The incorporation of DWT prior to the training of generative adversarial networks makes the image to be input closer to the Ground Truth image.
- The proposed method achieves the state-of-the-art performance on multiple benchmark datasets.

The rest of this paper is organized as follows: Section 2 describes the deep learning method for document image binarization. Section 3 introduces a novel three-stage generative adversarial networks method. Section 4 presents the experiments performed on this work, and compares the performance of our method and other methods on several benchmark datasets. Finally, Section 5 discusses the conclusion and the future work of this paper.

2. Related Work

In previous researches focusing on document image binarization, the field is broadly divided into two categories: traditional image processing methods and deep learning-based semantic segmentation methods. However, traditional image processing binarization methods are always based on the pixel-level local threshold values, such as global binarization [6] and local adaptive binarization [5, 7]. These methods are not satisfactory when dealing with documents affected by excessive interference or degradation [17, 18].

With the advancement of deep learning, the convolutional neural network (CNN) framework [19, 20] has become the predominant backbone of computer vision tasks. Within computer vision, semantic segmentation is one of the most important research topics, encompassing document image binarization. For instance, Tensmeyer *et al.* [10] employed pseudo-F-measure (p-FM) and F-measure (FM) losses during the training of FCN to apply the model to the document image binarization task. Ronneberger *et al.* [21] extended FCN, presenting the U-Net architecture, which captures contextual and spatial information through its distinctive U-shaped design. Inspired by this, Peng *et al.* [22] introduced an encoder-decoder architecture for document image binarization, where the decoder transforms the low-resolution representation to the original dimensions, resulting in the binarized image. Vo *et al.* [23] first applied hierarchical deep supervised network (DSN) to document image binarization and achieved the state-of-the-art (SOTA) performance on several benchmark datasets. He *et al.* [24] proposed an iterative deep learning framework applied to document image binarization and the trained model achieved excellent performance.

In recent years, generative adversarial networks (GANs) [25] have achieved exciting results in the generation of real-world images. Unlike GANs which generate output images from random noise, Isola *et al.* [26] proposed Pix2Pix GAN based on conditional GAN (cGAN) [27] for image-to-image translation. To ensure that the generated images are more realistic, Pix2Pix GAN employs generators for loss function optimization. Within the network architecture, the generator evaluates the minimized generated image against the target output image, quantifying the $L1$ loss between them. Meanwhile, the discriminator assesses the credibility of the generated image, relying on the input image and the reference target image. This process is depicted by the subsequent equation:

$$\arg \min_G \max_D V(G, D) = \mathbb{E}_x[\log(1 - D(x, G(x)))] + \mathbb{E}_{x,y}[\log D(x, y)] + \lambda \mathbb{E}_{x,y}[||y - G(x)||_1] \quad (1)$$

where the input data distribution \mathbb{P}_x samples the input image x ; the ground truth image of the input image is y , and the hyperparameter to increase the model regularization effect is λ . Generator G generates the input image as the generated image $G(x)$. From Eq. (1), the loss function between the generated image and the ground truth image is $L1$ instead of $L2$, which is beneficial to reduce blurring and ambiguity in the generation process.

Bhunja *et al.* [28] performed document image enhancement on the DIBCO dataset and used cGAN [27] for image binarization. Inspired by Pix2Pix GAN [26], Zhao *et al.* [29] proposed a cascade generator structure for document image binarization based on Pix2Pix GAN to solve the problem of multi-scale information combination. De *et al.* [30] designed two discriminators to combine local and global information. Suh *et al.* [31] set up a two-stage generative adversarial network for image binarization using Patch GAN [26]. These methods keep breaking the SOTA performance on DIBCO datasets.

3. Proposed Method

3.1. Overall Network Architecture

Considering the complexity of color document image degradation and the advantages [31] of processing different color channels separately, our proposed method divides the overall network architecture into three stages, which focus on enhancing image quality of degraded color documents and extracting text information from the images. In Stage-1, we use DWT and normalization to preprocess the patches of the input image. These preprocessed image patches are employed to train as the input of the generator within the adversarial network framework. Stage-2 focuses on the elimination of background color noise and the extraction of color foreground information, while Stage-3 involves the fusion of local and global predictions to produce the final output. The detailed introduction of each stage can be found in Sections 3.2, 3.3, and 3.4, respectively.

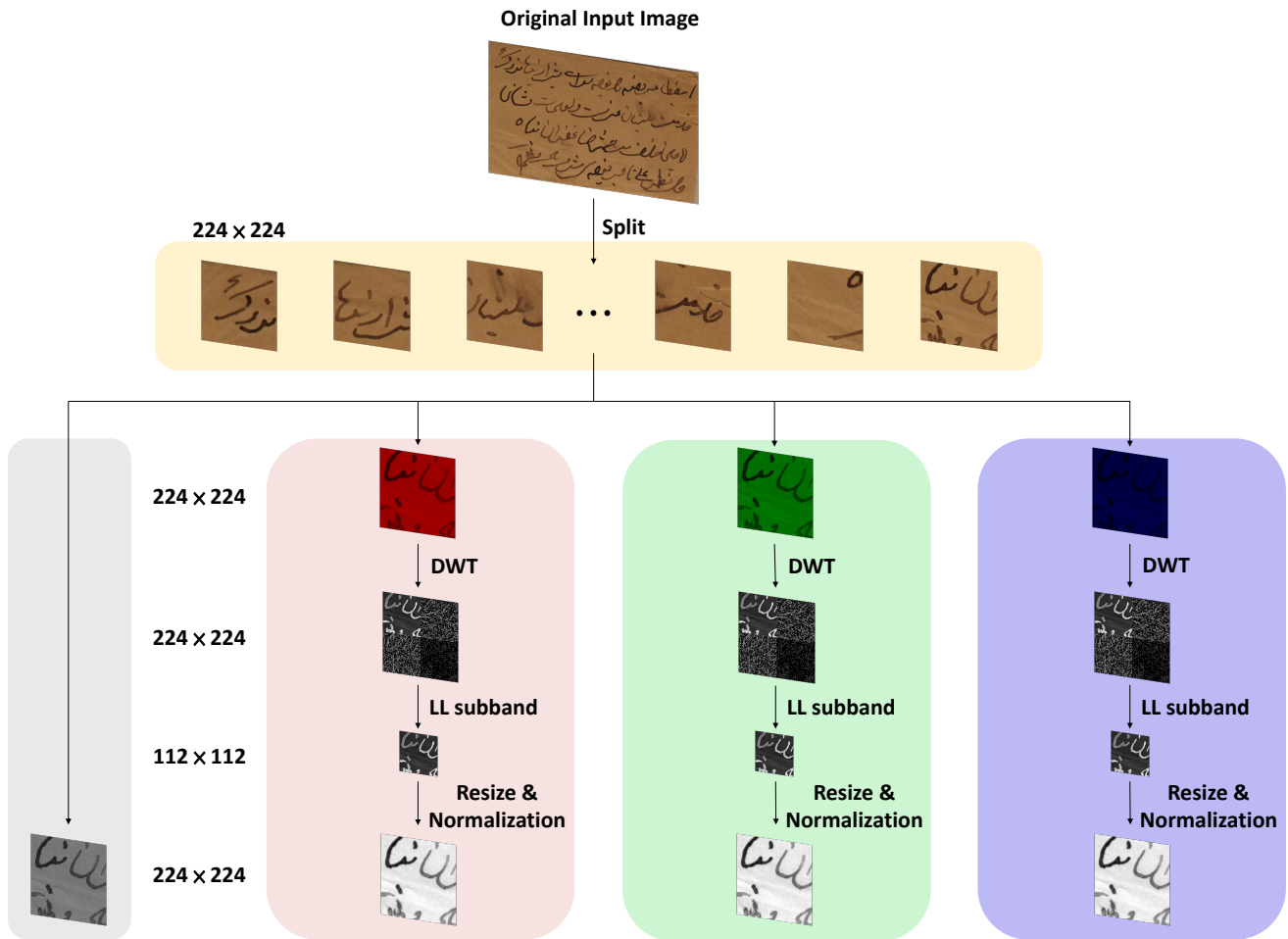


Figure 1: The architecture of Stage-1 of the proposed method. The original input image is divided into patches of 224×224 size, and split into grayscale images and RGB three single-channel images. The single-channel images are all in grayscale. However, to visually represent the different channels of the image separately, the single-channel images in this diagram are replaced with images in three different RGB colors.

3.2. Stage-1

This work employs four different generators to extract foreground color information from degraded document images while eliminating the background color. To preprocess the input of the different generators, we first split the original color image (24-bit) into RGB three single-channel images (8-bit) and one grayscale image (8-bit).

The ground truth (GT) image provided by the dataset is a single-channel binary image (8-bit), where pixel points have values of 0 for characters and 1 for the background. Images with varying channel numbers cannot be directly put into the discriminator for processing. As shown in Figure 1, we first split the RGB three channels of the original input image to create three single-channel RGB images. Then we apply DWT to each single-channel image, and retain the LL subband images for normalization. The GT images and the preprocessed grayscale images are summed at pixel wise as the corresponding ground truth images. Since the sizes of the retained LL subband images are 112×112 (half of the

224×224 length and width), we resize the images to the designated size of 224×224 using bicubic interpolation [32].

3.2.1. Discrete Wavelet Transform

In this work, we use Haar wavelet transform [33], which is one of the DWT, to process the input image. This process can be conceived as a bandpass filter, selectively allowing signals with frequencies akin to those of the wavelet basis function to traverse. The flowchart of this DWT processing is illustrated in Figure 2, which generates four subband images: one low-frequency subband image and three high-frequency subband images. This work takes the single-channel split images as input and processes the n -direction by low-pass filtering, as shown in the following equation:

$$v_L[m, n] = \sum_{k=0}^{K-1} x[m, 2n - k]g[k] \quad (2)$$

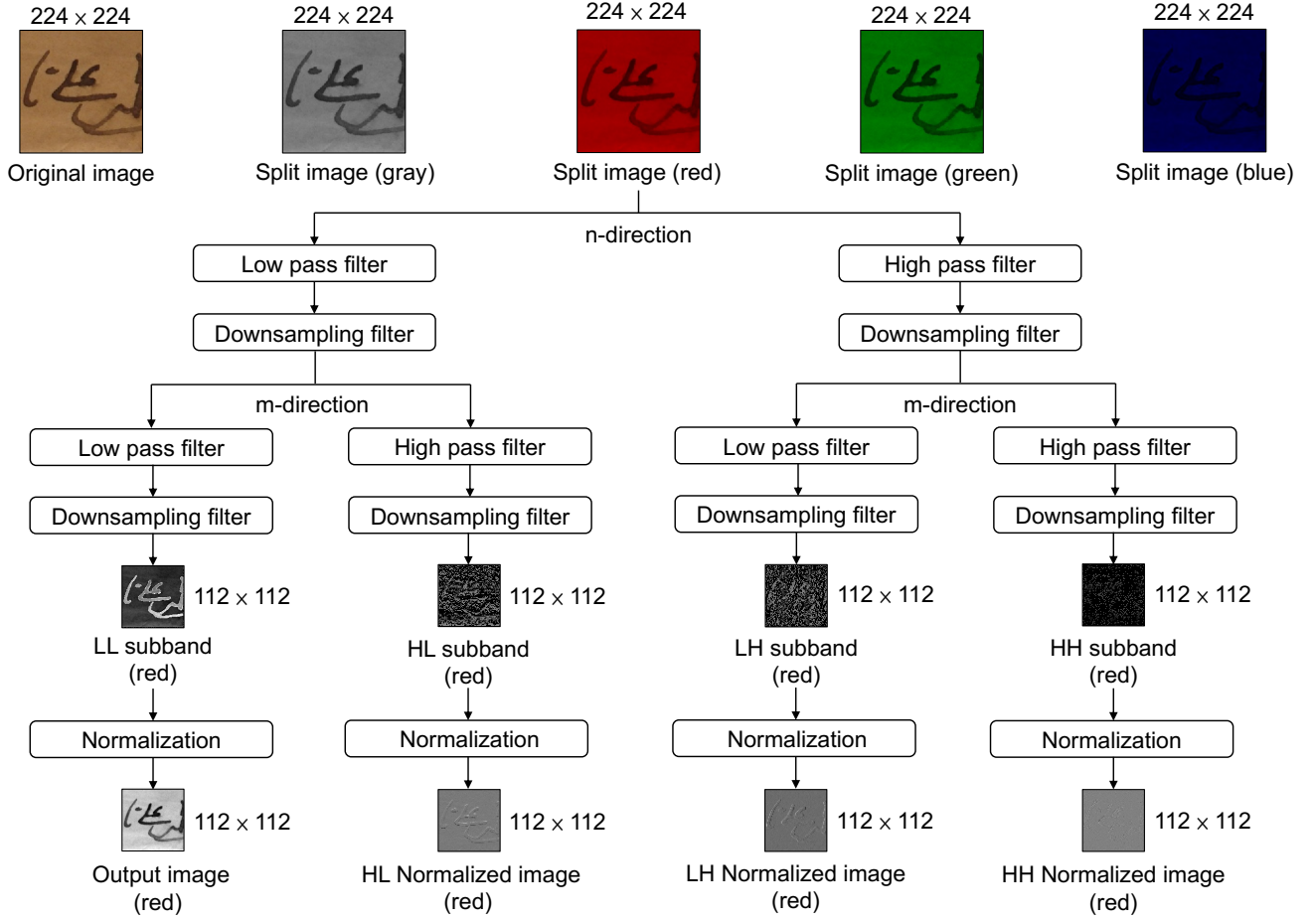


Figure 2: The architecture of the Haar wavelet transform used by the proposed method, which takes the red single-channel image patch as an example. The processes of the transform of the green and blue single-channel image patches are the same.

Next, this work uses the low-pass filtering applied to the m -direction of Eq. (2) to obtain the following equation:

$$v_{LL}[m, n] = \sum_{k=0}^{K-1} v_L[2m - k, n]g[k] \quad (3)$$

In contrast to the ground truth images provided by the dataset, the RGB single-channel images split from the original input images exhibit some substantial noise. This noise prevents them from being used directly in generating corresponding ground truth images through the generator and could potentially disrupt the performance of the trained adversarial network. DWT decomposes the image into both low-frequency and high-frequency information. The low-frequency component represents the mean value and the high-frequency component represents the difference value. The mean value, classified as low-frequency information, captures gradual changes and encodes both the picture's contour information and approximate details. Conversely, the difference value, characterized as high-frequency information, captures rapid changes and encodes intricate picture details as well as local information (including noises). Therefore, we apply DWT and retain the LL subband images

to input Stage-2, as shown in Figure 2, which effectively preserves contour information and reduces noise interferences.

3.2.2. Normalization

Normalization entails constraining data within a desired range, with the goal of simplifying the data processing and expediting convergence. The proposed equation for this process is expressed as:

$$I_N = (IV_{nmax} - IV_{nmin}) \frac{1}{1 + e^{-\frac{I-\beta}{\alpha}}} + IV_{nmin} \quad (4)$$

where IV is the intensity values, the image to be processed $I : \{\mathbb{X} \subseteq \mathbb{R}^n\} \rightarrow \{IV_{min}, \dots, IV_{max}\}$, and the generated image $I_N : \{\mathbb{X} \subseteq \mathbb{R}^n\} \rightarrow \{IV_{nmin}, \dots, IV_{nmax}\}$. α defines the width of the input intensity range, and β defines the range centered intensity.

In the proposed method, we normalize the LL subband images to present initially incomparable data for comparison. The reason we choose the normalized LL subband image as the output is shown in Figure 3, where we apply DWT and normalization to each subband images.

The illustrative example of the impact of normalization on RGB single-channel images after the DWT operation is

	LL Normalized Image	HL Normalized Image	LH Normalized Image	HH Normalized Image
Red				
Green				
Blue				

Figure 3: Results of Haar wavelet transform & normalization of RGB single-channel images split from the example image patches.

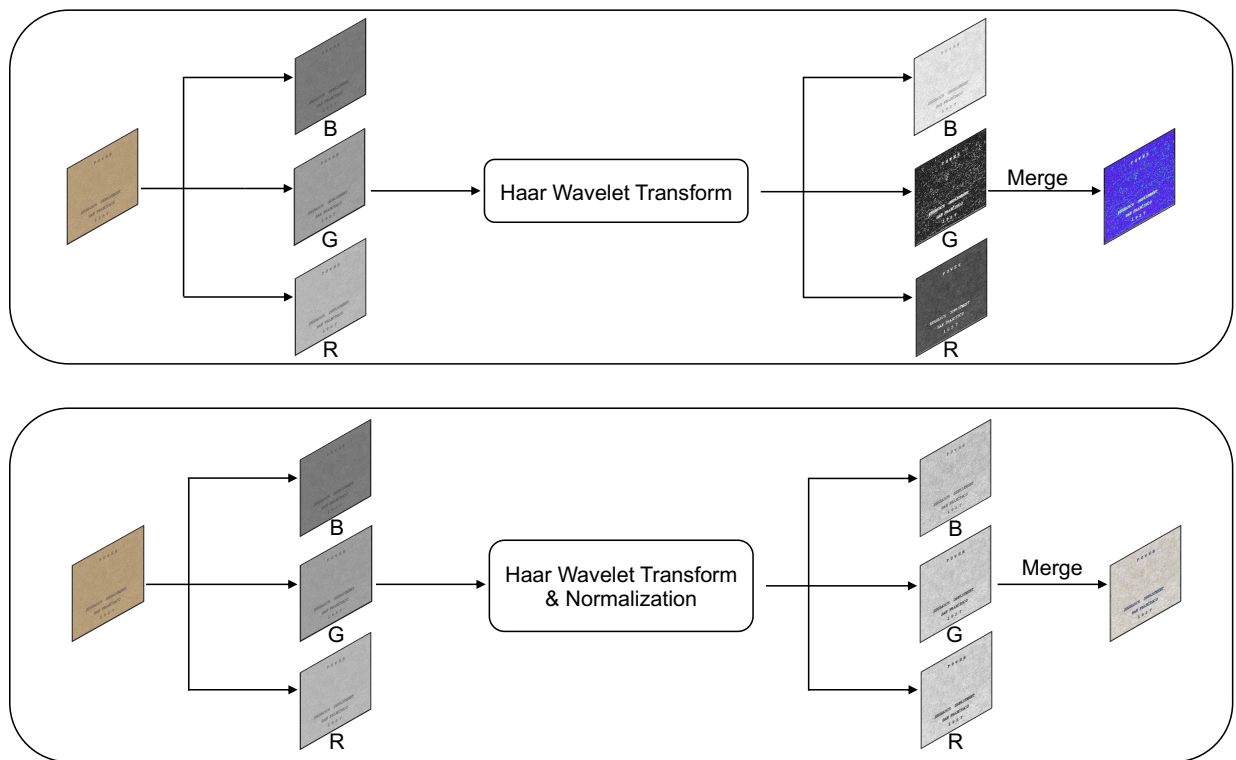


Figure 4: Image normalization from image HW15 of DIBCO 2011 dataset, the above is an example of no normalization after DWT retains LL subband images, whereas the below is the example of normalization after DWT retains LL subband images.

provided in Figure 4, when applied to image HW15 from the DIBCO 2011 dataset, normalization effectively balances the RGB. In contrast, without applying normalization results in an output image, it heavily skews towards the blue component. In addition, we also show that the global binarization results of the images using normalization are more similar to the Ground Truth images provided by the dataset compared to the images only processed by DWT, and the experiments are explained in detail in Section 4.5.

3.3. Stage-2

In Stage-2, the proposed method is illustrated in Figure 5. Initially, the original input images are split into three RGB single-channel images and one grayscale image. Each of the single-channel images is input into an independent generator, resulting in the use of four generators in Stage-2 of the proposed method. These four generators train the model separately, enabling this method to remove background information from the localized image blocks while extracting

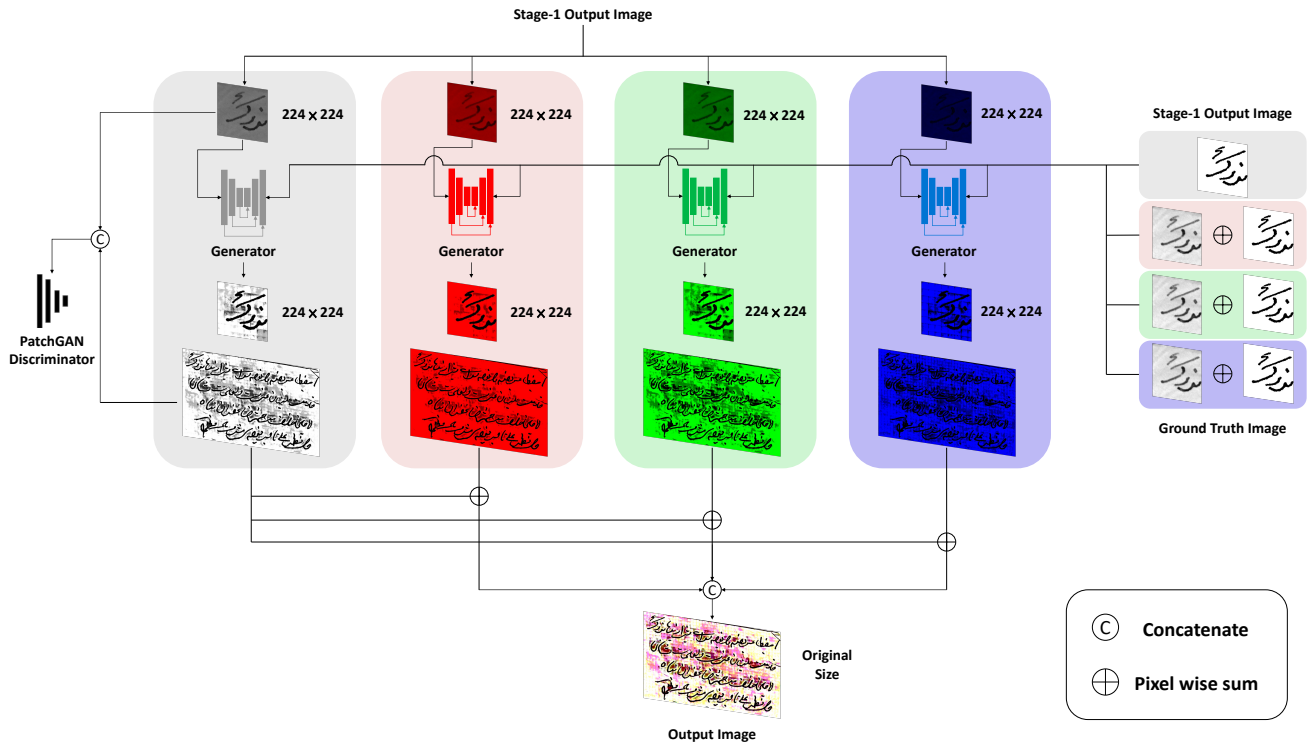


Figure 5: The architecture of Stage-2 of the proposed method. This method employs the U-Net++ [34, 35] architecture with EfficientNet-B6 [36] as the generator and improved PatchGAN [26] as the discriminator. The ground truth image during the training process is obtained from pixel-wise summation of the dataset provided image and the output from Stage-1.

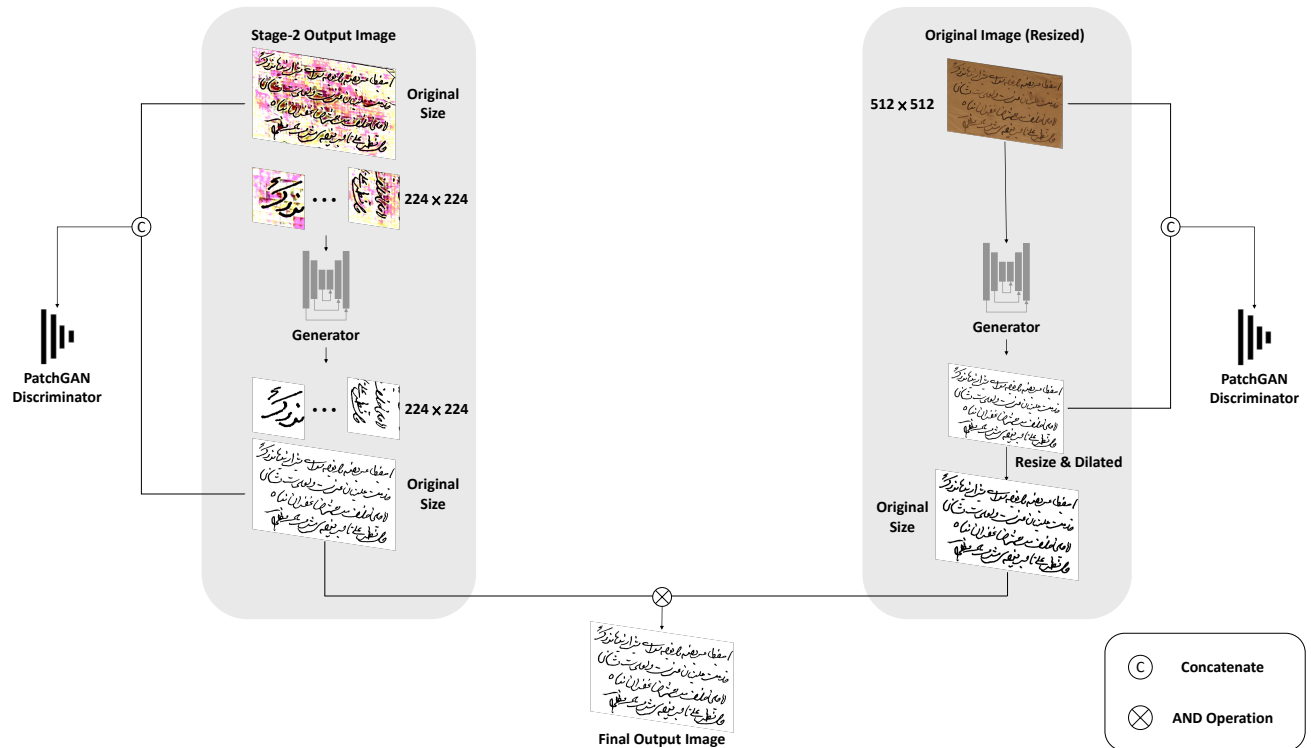


Figure 6: The architecture of Stage-3 of the proposed method. This stage comprises both local and global predictions. The local prediction involves training several 224×224 image patches, while the global prediction involves directly resizing the original image to 512×512 for training.

colored foreground details. Additionally, all single-channel images share the same discriminator to distinguish between the generated image and its corresponding ground truth image.

3.3.1. Loss functions of GAN

To ensure a more robust convergence of the loss function, we follow the improved Wasserstein generative adversarial network with gradient penalty (WGAN-GP) [37] used by Suh *et al.* [31] applied to the objective function. Experiments by Bartusiak *et al.* [38] have demonstrated that the binary cross-entropy (BCE) loss yields superior performance compared to the $L1$ loss in binary classification tasks. Therefore, we chose the BCE loss instead of the $L1$ loss used in the Pix2Pix GAN [26]. The loss function of the WGAN-GP, which incorporates the BCE loss, is formulated as follows:

$$\mathbb{L}_D = -\mathbb{E}_{x,y}[D(y,x)] + \mathbb{E}_x[D(G(x),x)] + \alpha \mathbb{E}_{x,\hat{y} \sim P_{\hat{y}}}[(\|\nabla_{\hat{y}} D(\hat{y},x)\|_2 - 1)^2] \quad (5)$$

$$\mathbb{L}_G = \mathbb{E}_x[D(G(x),x)] + \lambda \mathbb{E}_{G(x),y}[y \log G(x) + (1-y) \log(1-G(x))] \quad (6)$$

where the penalty coefficient is α , and the uniform sampling along a straight line between the ground truth distribution P_y and the point pairs of the generated data distribution is $P_{\hat{y}}$. λ is used to control the relative importance of different loss terms. In the discriminator, the generated image is distinguished from the real image by the loss function \mathbb{L}_D in Eq. (5). In the generator, the distance between the generated image and the ground truth image in each color channel is minimized by the loss function \mathbb{L}_G in Eq. (6).

3.3.2. Network architecture

Given the unpredictability of color document degradation, this work adopts four independent adversarial networks to extract text information from diverse colored backgrounds. This method mitigates color interference during document image binarization.

For the network proposed in Stage-2, four independent generators apply the same encoder-decoder architecture. The encoder extracts features, while a shared decoder is employed by multiple encoders of varying depths, and subsequently the features are concatenated. A skip connection is used between the encoder and the decoders. The encoder facilitates downsampling and context extraction, while the decoders undertake upsampling and amalgamate both upscaled and downsampled features. Specifically, this work employs EfficientNet-B6 [36] as the encoder, which is a lightweight CNN known for its performance in image classification tasks. For the discriminator, we choose the one [26, 29, 30, 39, 40, 41] used by Suh *et al.* [31] due to its superior generalization capabilities. Additionally, instead of U-Net [21] used by Suh *et al.* [31], this work uses its improved model U-Net++ [34, 35] for semantic segmentation, which can further improve the model performance.

The detailed procedure for training the proposed GAN models is illustrated in Algorithm 1. The training process is conducted in our training environment, which is described in Section 4.3, encompassing optimizer selection, learning rate configuration, and loss function definition. The algorithm demonstrates that the GAN model iteratively updates the loss function based on the authenticity assessment of the generated image by the discriminator. This iterative process enhances the ability of the generator to produce more real images.

Algorithm 1 Training process for the proposed GAN models

Require: Input images I_{input}
Ensure: $\omega = 0.5, \alpha = 10, \lambda = 50, \eta = 1 \times 10^{-4}$

- 1: **Initialize:** Parameters $\theta_{G_r}, \theta_{G_g}, \theta_{G_b}, \theta_{G_{gray}}$
- 2: **for** number of training iterations **do**
- 3: Split I_{input} into $\{red, green, blue, gray\}$ images
- 4: **for** $k = \{red, green, blue, gray\}$ **do**
- 5: **if** k is gray **then**
- 6: $y_k \leftarrow y$
- 7: **else**
- 8: $x'_k = Norm(V_{LL}(x_k))$
- 9: $y_k \leftarrow x'_k \cap y$
- 10: Binarize y_k with threshold value t .
- 11: **end if**
- 12: Update Discriminator D (Eq. (5)):
- 13: $\theta_D \leftarrow \theta_D - \eta_D \nabla_{\theta_D} \mathbb{L}_D$
- 14: Update Generator G_k (Eq. (6)):
- 15: $\theta_{G_k} \leftarrow \theta_{G_k} - \eta_G \nabla_{\theta_{G_k}} \mathbb{L}_G$
- 16: **end for**
- 17: **end for**
- 18: **for** $k = \{red, green, blue\}$ **do**
- 19: $\hat{y}_k \leftarrow \omega G_k(x_k) + (1-\omega)G_{gray}(x_{gray})$
- 20: **end for**
- 21: $\hat{y} \leftarrow [\hat{y}_r, \hat{y}_g, \hat{y}_b]$

3.4. Stage-3

In Stage-3, a multi-scale adversarial network is employed to generate images for both local and global binarization results, enhancing the distinction between the background and text with higher accuracy. Contrary to Stage-2, which predominantly relies on local prediction using the image patches (224×224), Stage-3 conducts global prediction on the resized input image (512×512). This method reduces the contextual information loss in text caused by the local predictions of Stage-2.

Figure 6 illustrates the process of two independent discriminators in Stage-3. Different from Stage-2 using 8-bit images for local prediction, Stage-3 uses 24-bit images as the input of the generator. Additionally, Figure 6 clarifies that the left-side input image comprises the image patches from the Stage-2 output, intended for local prediction. Conversely, the right-side input image represents the resized image from the original input for global prediction. In the binarization process of Stage-3, the network architecture of the generator

remains consistent with Stage-2, differing only in the number of input channels.

4. Experiments

4.1. Datasets

4.1.1. DIBCO

The Document Image Binarization Competition (DIBCO) provides several datasets: DIBCO 2009 [42], H-DIBCO 2010 [43], DIBCO 2011 [11], H-DIBCO 2012 [44], DIBCO 2013 [12], H-DIBCO 2014 [13], H-DIBCO 2016 [14], DIBCO 2017 [15], and H-DIBCO 2018 [16]. These datasets comprise both grayscale and color images, including machine-printed as well as handwritten content. Participants in the competition were tasked with designing algorithms capable of extracting binarized text images from both handwritten and machine-printed images within these datasets.

4.1.2. PHIBD

The Persian Heritage Image Binarization Dataset (PHIBD) [45] contains 15 images of historical manuscripts from Mirza Mohammad Kazemai's old manuscript library in Yazd, Iran. The images within the dataset have suffered from various types of degradation.

4.1.3. SMADI

The Synchromedia Multispectral Ancient Document Images Dataset (SMADI) [1] consists of 240 multispectral images of 30 authentic historical handwritten letters. These letters, dating from the 17th to the 20th centuries, were written using iron gall ink. The original documents are deposited at the BANQ Bibliotheque et Archives nationales du Quebec. A total of 240 images of real documents were meticulously captured, calibrated, and registered within this dataset. Each of these images was imaged with a CROMA CX MSI camera, resulting in 8 images per document.

4.1.4. Bickley Diary Dataset

The Bickley Diary Dataset (BD) [46] has been generously donated to the Singapore Methodist Archives by Erin Bickley. This dataset comprises diaries in which the images have been affected by both light and fold damages, thereby complicating the process of identification.

4.2. Evaluation Metric

In comparison with other traditional and SOTA methods for document image binarization, based on the case that DIBCO datasets do not provide OCR output, we use the following five evaluation metrics:

4.2.1. F-measure (FM)

$$FM = \frac{2 \times \text{Recall} \times \text{Precision}}{\text{Recall} + \text{Precision}} \quad (7)$$

where the Recall is defined as $\frac{TP}{TP+FN}$; the Precision is defined as $\frac{TP}{TP+FP}$, and TP, FP, and FN represent the true

positive, false positive, and false negative values, respectively.

4.2.2. Pseudo-F-measure (p-FM)

$$p-FM = \frac{2 \times \text{Recall}_{ps} \times \text{Precision}_{ps}}{\text{Recall}_{ps} + \text{Precision}_{ps}} \quad (8)$$

where the Pseudo-Recall (Recall_{ps}) and the Pseudo-Precision (Precision_{ps}) both use the distance weights relative to the ground truth image profile to generate a new weighted ground truth image.

4.2.3. Peak signal-to-noise ratio (PSNR)

$$PSNR = 10 \log\left(\frac{V^2}{MSE}\right) \quad (9)$$

where V represents the difference between the foreground and background, and the Mean Square Error (MSE) is defined as:

$$MSE = \frac{\sum_{x=0}^{M-1} \sum_{y=0}^{N-1} [L(x, y) - L'(x, y)]^2}{M \times N} \quad (10)$$

where M and N are the total number of pixels of image L and image L' respectively. Generally, a higher PSNR value indicates greater similarity between the images.

4.2.4. Distance reciprocal distortion (DRD)

DRD represents a measure of visual distortion in the binary image, which is shown in the following equation:

$$DRD = \frac{\sum_k DRD_k}{NUBN} \quad (11)$$

where NUBN corresponds to the number of uneven 8×8 blocks in the ground truth image, and DRD_k is defined as:

$$DRD_k = \sum_{i=-2}^2 \sum_{j=-2}^2 |G_k(i, j) - B_k(x, y)| \times N_w(i, j) \quad (12)$$

where DRD_k indicates the distortion of the k_{th} flipped pixel, calculated using a 5×5 normalized weight matrix N_w . B_k refers to the pixel of the binary image, and G_k denotes the pixel of the ground truth image.

4.2.5. Avg-Score (Avg)

The Peak Signal-to-Noise Ratio (PSNR) provides a straightforward and intuitive quantitative metric for comparing the generated image with the ground truth image. Although it can be used as a supplementary metric, it should not be the only evaluation measure. The F-measure and p-F-measure are used to assess the accuracy of different methods, but a higher value in these metrics does not always correspond to a higher PSNR value. In our experiments, it is common to observe that a method achieves the SOTA PSNR value, while the F-measure and p-F-measure values

Table 1

Comparison of the PSNR values of the images from different training sets that have been processed using different methods with the corresponding ground truth images.

Method	DIBCO 2009	H-DIBCO 2010	H-DIBCO 2012	Bickley Diary	PHIBD	SMADI	Mean Values
Original Input	63.2879	61.3446	61.8542	57.6995	60.7355	61.2175	61.0232
DWT	64.1154	71.4422	64.8151	53.7037	51.5094	60.1374	60.9539
DWT&Norm	80.4286	86.1904	82.4625	74.2314	83.6403	78.5337	80.9145

Table 2

Quantitative comparison (FM/p-FM/PSNR/DRD/Avg) of the models trained with different patch sizes ($224 \times 224/256 \times 256$) on multiple benchmark datasets.

	DIBCO 2011	DIBCO 2013	H-DIBCO 2014	H-DIBCO 2016	DIBCO 2017	DIBCO 2018	Mean Values
256×256	FM \uparrow	94.11	95.06	96.62	91.40	90.95	93.32
	p-FM \uparrow	96.97	97.30	98.01	96.22	93.97	96.37
	PSNR \uparrow	20.48	22.16	22.25	19.63	18.55	20.51
	DRD \downarrow	1.76	1.66	0.96	2.96	2.95	2.17
	Avg \uparrow	77.45	78.22	78.98	76.07	75.13	77.01
224×224	FM \uparrow	94.22	94.65	96.60	91.76	91.31	93.57
	p-FM \uparrow	97.47	97.10	98.33	96.82	94.30	96.83
	PSNR \uparrow	20.54	22.01	22.23	19.73	18.63	20.59
	DRD \downarrow	1.69	1.98	0.97	2.81	2.88	2.09
	Avg \uparrow	77.64	77.95	79.05	76.38	75.34	77.22

are lower than those of other models. To solve this problem, we followed the Avg-Score metric used by Jemni *et al.* [47] to compare the combined performance of different methods, as shown in the following equation:

$$Avg = \frac{FM + p-FM + PSNR + (100 - DRD)}{4} \quad (13)$$

4.3. Implementation Details

4.3.1. Data preparation

The performance of a neural network depends on the quality and quantity of its training data. In general, the more training data enhances the better the performance of the neural network. To compare the performance of the proposed method with other methods, we follow the strategy described in [23, 24, 31] for constructing the training and test sets. Specifically, the training set includes a total of 143 images from DIBCO 2009 [42], H-DIBCO 2010 [43], H-DIBCO 2012 [44], PHIBD [45], SMADI [1], and BD [46] dataset. The test sets comprise a total of 82 images from DIBCO 2011 [11], DIBCO 2013 [12], H-DIBCO 2014 [13], H-DIBCO 2016 [14], DIBCO 2017 [15], and H-DIBCO 2018 [16].

To ensure a fair comparison of performance among all methods, we used the same data augmentation for our method and other SOTA methods. During the training process of the local prediction network, this work splits the input images into patches with 224×224 in size. These patches were sampled with scale factors of 0.75, 1.25, 1.5, subsequently resized to 224×224 , and rotated by 270° . In contrast, for training the global prediction network, this work

employed scaling without rotation for data augmentation, using a scaling size of 512×512 . To diversify the training data, rotation augmentation was applied to the global prediction, involving rotations of 90° , 180° , and 270° , as well as horizontal and vertical flips.

4.3.2. Training

The experiments were conducted using the PyTorch framework in Python. We use NVIDIA RTX 3090 GPUs for all the following experiments.

In this study, we employ the generator comprising EfficientNet-B6 [36] with UNet++ [34, 35]. Regarding the training hyperparameters, Stage-2 and Stage-3 share similar settings, differing primarily in the number of training epochs: 150 epochs for global prediction and 10 epochs for the remaining networks. The choice of optimizer was Adam [49], with a learning rate set at 2×10^{-4} . Additionally the generator employed $\beta_1 = 0.5$, while the discriminator used $\beta_2 = 0.999$.

4.3.3. Pre-training

To enhance training efficacy due to limited data availability, we employed EfficientNet-B6 [36] as the encoder in the generator, utilizing weights pretrained on the ImageNet dataset [50].

4.4. Comparison with other Methods

In our previous conference paper [51], we compared various deep learning-based methods and found that some of these methods [10, 28, 29] employed a ‘‘leave-one-out’’ strategy for selecting the training set. For instance, when the DIBCO 2013 dataset is used as the test set, all other

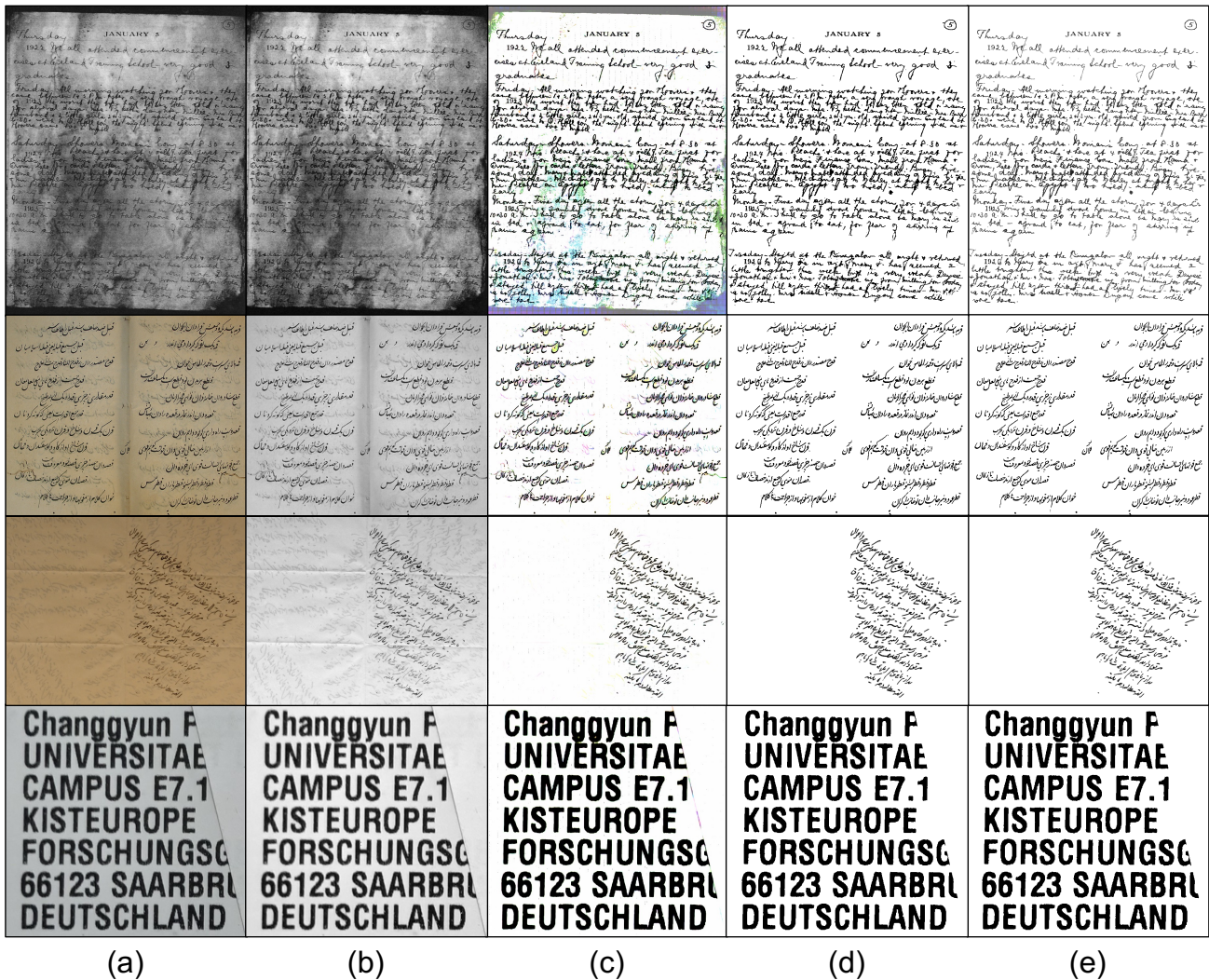


Figure 7: Visualization examples of the results of the proposed method at each stage. (a) the original input images, (b) the LL subband images obtained by Haar wavelet transform and normalization (Stage-1), (c) the enhanced images produced using our image enhancement method (Stage-2), (d) the binarized images obtained by combining local and global predictions (Stage-3), (e) the ground truth images.

datasets are utilized as the training set. Although our method still demonstrates superior performance at the SOTA level in such case [51], we consider it unfair to compare them directly because our model uses a smaller training set. Therefore, this work excludes these methods from this paper and only retains those that use the exact same training set for comparison.

4.5. Image Enhancement Experiment

In Stage-1, we applied DWT and normalization to the original input images. While mathematical theory [52] suggests that these processed images can retain contour information and reduce noise more efficiently, it is important to demonstrate their impact on experimental results. The previous conference paper [51] on this work presented ablation experiments on DWT and normalization. Based on this, it is better to intuitively show that, compared to the original input

images, the DWT and normalization processed images are closer to the ground truth images.

In Stage-1 of this work, we set the threshold to 0.3 to binarize different single-channel images to obtain corresponding binarized images. In the experiment of this section, we applied the above image binarization to the original input images, the images processed with DWT, and the images processed with both DWT and normalization. Subsequently, we calculated the PSNR values of the binarized images compared to the ground truth images using these three methods, and the results are presented in Table 2. The PSNR mean values of the original input images are 61.0232. In contrast, the PSNR mean values of the images after DWT processing are slightly lower at 60.9539. However, the PSNR mean values of the images processed with both DWT and normalization are 80.9145, which means they are closer to the ground truth images. This demonstrates that it is more reasonable to choose the DWT and normalization processed

Table 3

Comparison of performance evaluation of the proposed method and other methods for document binarization on multiple benchmark datasets. Best and 2nd best performance are in **red**

and **blue** colors, respectively. The data for the experimental results of other methods are obtained from [31, 48].

(a) DIBCO 2011						(b) DIBCO 2013					
Method	FM↑	p-FM↑	PSNR↑	DRD↓	Avg↑	Method	FM↑	p-FM↑	PSNR↑	DRD↓	Avg↑
Niblack [5]	70.44	73.03	12.39	24.95	57.73	Niblack [5]	71.38	73.17	13.54	23.10	58.75
Otsu [6]	78.60	80.53	15.31	22.57	62.97	Otsu [6]	80.04	83.43	16.63	10.98	67.28
Sauvola [7]	85.37	89.08	16.37	7.08	70.94	Sauvola [7]	82.71	87.74	17.02	7.64	69.96
Howe [17]	94.04	95.06	20.43	2.10	76.86	Howe [17]	91.34	91.79	21.29	3.18	75.31
Jia [18]	93.17	95.32	19.44	2.29	76.41	Jia[18]	93.28	96.58	20.76	2.01	77.15
Vo [23]	92.58	94.67	19.16	2.38	76.01	Vo [23]	93.43	95.34	20.82	2.26	76.83
He [24]	91.92	95.82	19.49	2.37	76.22	He [24]	93.36	96.70	20.88	2.15	77.20
Suh [31]	93.57	95.93	20.22	1.99	76.93	Suh [31]	95.01	96.49	21.99	1.76	77.93
Ours	94.22	97.47	20.54	1.69	77.64	Ours	94.65	97.10	22.01	1.98	77.95

(c) H-DIBCO 2014						(d) H-DIBCO 2016					
Method	FM↑	p-FM↑	PSNR↑	DRD↓	Avg↑	Method	FM↑	p-FM↑	PSNR↑	DRD↓	Avg↑
Niblack [5]	86.01	88.04	16.54	8.26	70.58	Niblack [5]	72.57	73.51	13.26	24.65	58.67
Otsu [6]	91.62	95.69	18.72	2.65	75.85	Otsu [6]	86.59	89.92	17.79	5.58	72.18
Sauvola [7]	84.70	87.88	17.81	4.77	71.41	Sauvola [7]	84.64	88.39	17.09	6.27	70.96
Howe [17]	96.49	97.38	22.24	1.08	78.76	Howe [17]	87.47	92.28	18.05	5.35	73.11
Jia [18]	94.89	97.68	20.53	1.50	77.90	Jia [18]	90.10	93.72	19.00	4.03	74.70
Vo [23]	95.97	97.42	21.49	1.09	78.45	Vo [23]	90.01	93.44	18.74	3.91	74.57
He [24]	95.95	98.76	21.60	1.12	78.80	He [24]	91.19	95.74	19.51	3.02	75.86
Suh [31]	96.36	97.87	21.96	1.07	78.78	Suh [31]	92.24	95.95	19.93	2.77	76.34
Ours	96.60	98.33	22.23	0.97	79.05	Ours	91.76	96.82	19.73	2.81	76.38

(e) DIBCO 2017						(f) DIBCO 2018					
Method	FM↑	p-FM↑	PSNR↑	DRD↓	Avg↑	Method	FM↑	p-FM↑	PSNR↑	DRD↓	Avg↑
Otsu [6]	77.73	77.89	13.85	15.54	63.48	Otsu [6]	51.45	53.05	9.74	59.07	38.79
Sauvola [7]	77.11	84.10	14.25	8.85	66.65	Sauvola [7]	67.81	74.08	13.78	17.69	59.50
Howe [17]	90.10	90.95	18.52	5.12	73.61	Howe [17]	80.84	82.85	16.67	11.96	67.10
Jia [18]	85.66	88.30	16.40	7.67	70.67	Jia [18]	76.05	80.36	16.90	8.13	66.30
Suh [31]	90.95	94.65	18.40	2.93	75.27	Suh [31]	91.86	96.25	20.03	2.60	76.39
Ours	91.31	94.30	18.63	2.88	75.34	Ours	92.89	96.96	20.39	2.23	77.00

image rather than the original input image and the DWT processed image.

4.6. Comparison Experiment

To ensure fairness in the experiments, we used the same training set and data augmentation techniques described in Section 4.3.1 for all the compared models. Unlike Suh *et al.* [31], who split the input images into 256×256 patches, our proposed method uses 224×224 patches. To demonstrate the positive impact of this change on the model performance, we conducted experiments comparing models using 224×224 patches with those using 256×256 patches, keeping all other settings unchanged.

Table 2 presents the performance of the models across different patch sizes on six DIBCO datasets. As established in Section 4.5, the images processed with DWT and normalization outperform those processed with either the original

input images or only with DWT. Consequently, all models in this section utilize images processed with DWT and normalization. According to Table 2, the mean values of FM, p-FM, PSNR, DRD, and Avg for the model based on 224×224 patches are 93.57, 96.83, 20.59, 2.09, and 77.22, respectively, which are superior to those for the model based on 256×256 patches. This indicates that the model based on 224×224 patches performs better, and therefore we will use this model for subsequent comparisons.

4.7. Experimental Results

Different from the conference paper [51] of this work, which uses option 3 to train the model, the proposed method in this paper applies DWT and normalization to the images in Stage-1 as input to train the model. The performance of the trained model will then be compared with that of other methods.



Figure 8: Example of document image binarization results from input image HW1 of DIBCO 2011 dataset by different methods: (a) original input, (b) Otsu [6], (c) Niblack [5], (d) Sauvola [7], (e) Vo [23], (f) He [24], (g) Suh [31], (h) Ours, (i) ground truth.

Figure 7 presents the visualization results at each stage of the trained model. Specifically, five images were randomly selected from the PHIBD and Bickley Diary datasets to demonstrate the step-by-step process of image enhancement and binarization using the proposed method. Figure 7 (b)

represents the result of retaining the LL subband images after applying DWT and normalization. This stage performs noise reduction on the original input image, which is used as the ground truth image for the generator. Figure 7 (c) shows the result of image enhancement achieved using adversarial

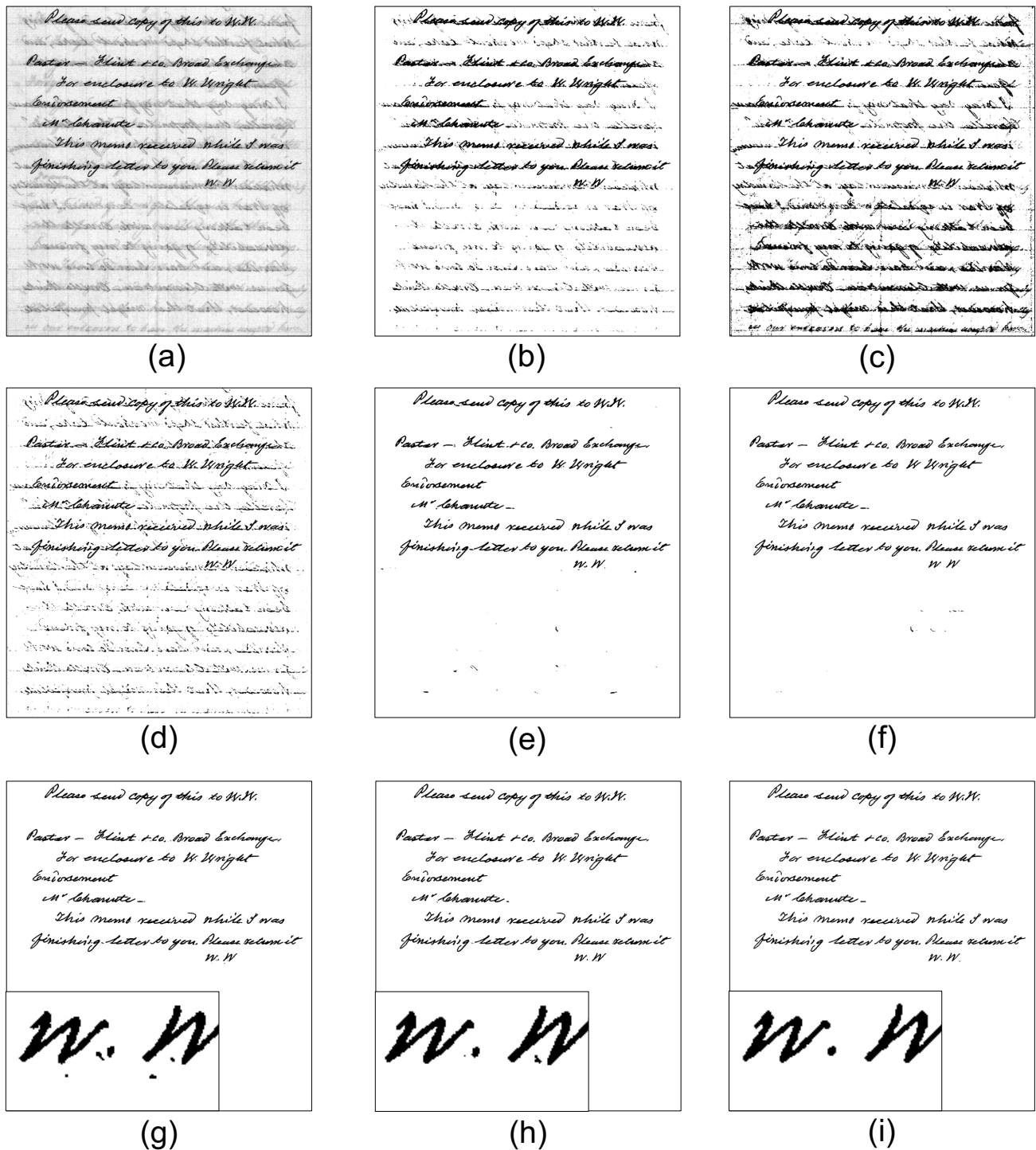


Figure 9: Example of document image binarization results from input image HW5 of DIBCO 2013 dataset by different methods: (a) original input, (b) Otsu [6], (c) Niblack [5], (d) Sauvola [7], (e) Vo [23], (f) He [24], (g) Suh [31], (h) Ours, (i) ground truth.

networks, where the image has the background color removed and the color of the text highlighted. Figure 7 (d) is the final output image obtained using the proposed whole method. Notably, it is evident that our final output result closely approximates Figure 7 (e), the ground truth image.

Table 3 presents the evaluation results of different models on six DIBCO datasets. Overall, the proposed method

achieves the top two best performance in terms of FM, p-FM, PSNR, and DRD, with its Avg value reaching the SOTA level across all six datasets. Notably, the performance of the proposed method on the DIBCO 2011 and 2013 datasets is particularly good, obtaining the best values for each of the evaluated metrics. For instance, on the DIBCO 2011 dataset, the p-FM value of the proposed method is 97.47,

significantly surpassing the second best value of 95.93. Similarly, on the DIBCO 2018 dataset, the FM value of the proposed method is 92.89, considerably higher than the second best value of 91.86. These results indicate that the proposed method is more effective than other methods for the binarization of degraded color documents.

In addition to assessing method performance by comparing quantitative metrics across various methods, this work aims to provide readers with an intuitive understanding of the distinctions by the visualization results. Consequently, we have chosen images from the DIBCO 2011 and 2013 datasets to illustrate examples of binarization results. Figures 8 and 9 show the binarization results of images HW1 and HW5 by different methods. These figures visually demonstrate that the proposed method outperforms deep learning based methods and the traditional binarization methods in terms of the shadow and noise elimination. Furthermore, the proposed method is good at preserving textual content while effectively mitigating the presence of the shadows and noise.

5. Conclusion

This paper introduces a novel three-stage method based on DWT and GANs to apply the task of text degradation in degraded document images with color backgrounds. The proposed method involves preserving the LL subband images through DWT to eliminate image noise, serving as the ground truth images for the generator. It trains independent networks utilizing RGB three single-channel images and one grayscale image, followed by a fusion of local and global prediction networks for binarization. As far as our knowledge extends, this work first represents the three-stage method that combines traditional image processing with deep learning for document binarization. The experimental results demonstrate that employing U-Net++ with EfficientNet-B6 as the generator and PatchGAN as the discriminator outperforms performance compared to other SOTA methods.

6. Declarations

This paper is an expanded paper from 20th Pacific Rim International Conference on Artificial Intelligence (PRICAI) held on November 15-19, 2023 in Jakarta, Indonesia.

6.1. Declaration of Funding

This research is supported by National Science and Technology Council of Taiwan, under Grant Number: NSTC 112-2221-E-032-037-MY2.

6.2. Declaration of competing interest

The authors have no financial or proprietary interests in any material discussed in this article.

6.3. Declaration of Generative AI and AI-assisted technologies in the writing process

The authors only use generative artificial intelligence (AI) and AI-assisted technologies to improve language.

References

- [1] R. Hedjam, M. Cheriet, Historical document image restoration using multispectral imaging system, *Pattern Recognition* 46 (8) (2013) 2297–2312.
- [2] B. Sun, S. Li, X.-P. Zhang, J. Sun, Blind bleed-through removal for scanned historical document image with conditional random fields, *IEEE Transactions on Image Processing* 25 (12) (2016) 5702–5712.
- [3] N. Kligler, S. Katz, A. Tal, Document enhancement using visibility detection, in: *Proceedings of the IEEE Conference on Computer Vision and Pattern Recognition*, 2018, pp. 2374–2382.
- [4] A. Sulaiman, K. Omar, M. F. Nasrudin, Degraded historical document binarization: A review on issues, challenges, techniques, and future directions, *Journal of Imaging* 5 (4) (2019) 48.
- [5] W. Niblack, *An introduction to digital image processing*, Strandberg Publishing Company, 1985.
- [6] N. Otsu, A threshold selection method from gray-level histograms, *IEEE transactions on systems, man, and cybernetics* 9 (1) (1979) 62–66.
- [7] J. Sauvola, M. Pietikäinen, Adaptive document image binarization, *Pattern recognition* 33 (2) (2000) 225–236.
- [8] J. Calvo-Zaragoza, A.-J. Gallego, A selectional auto-encoder approach for document image binarization, *Pattern Recognition* 86 (2019) 37–47.
- [9] J. Long, E. Shelhamer, T. Darrell, Fully convolutional networks for semantic segmentation, in: *Proceedings of the IEEE conference on computer vision and pattern recognition*, 2015, pp. 3431–3440.
- [10] C. Tensmeyer, T. Martínez, Document image binarization with fully convolutional neural networks, in: *2017 14th IAPR international conference on document analysis and recognition (ICDAR)*, Vol. 1, IEEE, 2017, pp. 99–104.
- [11] I. Pratikakis, B. Gatos, K. Ntirogiannis, Icdar 2011 document image binarization contest (dibco 2011), in: *2011 International Conference on Document Analysis and Recognition*, IEEE, 2011, pp. 1506–1510.
- [12] I. Pratikakis, B. Gatos, K. Ntirogiannis, Icdar 2013 document image binarization contest (dibco 2013), in: *2013 12th International Conference on Document Analysis and Recognition*, 2013, pp. 1471–1476. doi:10.1109/ICDAR.2013.219.
- [13] K. Ntirogiannis, B. Gatos, I. Pratikakis, Icfhr2014 competition on handwritten document image binarization (h-dibco 2014), in: *2014 14th International conference on frontiers in handwriting recognition*, IEEE, 2014, pp. 809–813.
- [14] I. Pratikakis, K. Zagoris, G. Barlas, B. Gatos, Icfhr2016 handwritten document image binarization contest (h-dibco 2016), in: *2016 15th International Conference on Frontiers in Handwriting Recognition (ICFHR)*, IEEE, 2016, pp. 619–623.
- [15] I. Pratikakis, K. Zagoris, G. Barlas, B. Gatos, Icdar2017 competition on document image binarization (dibco 2017), in: *2017 14th IAPR International Conference on Document Analysis and Recognition (ICDAR)*, Vol. 1, IEEE, 2017, pp. 1395–1403.
- [16] I. Pratikakis, K. Zagori, P. Kaddas, B. Gatos, Icfhr 2018 competition on handwritten document image binarization (h-dibco 2018), in: *2018 16th International Conference on Frontiers in Handwriting Recognition (ICFHR)*, IEEE, 2018, pp. 489–493.
- [17] N. R. Howe, Document binarization with automatic parameter tuning, *International journal on document analysis and recognition (ijdar)* 16 (2013) 247–258.
- [18] F. Jia, C. Shi, K. He, C. Wang, B. Xiao, Degraded document image binarization using structural symmetry of strokes, *Pattern Recognition* 74 (2018) 225–240.
- [19] M. D. Zeiler, R. Fergus, Visualizing and understanding convolutional networks, in: *European conference on computer vision*, Springer, 2014, pp. 818–833.
- [20] A. Krizhevsky, I. Sutskever, G. E. Hinton, Imagenet classification with deep convolutional neural networks, *Communications of the ACM* 60 (6) (2017) 84–90.
- [21] O. Ronneberger, P. Fischer, T. Brox, U-net: Convolutional networks for biomedical image segmentation, in: *International Conference on Medical image computing and computer-assisted intervention*,

- Springer, 2015, pp. 234–241.
- [22] X. Peng, H. Cao, P. Natarajan, Using convolutional encoder-decoder for document image binarization, in: 2017 14th IAPR international conference on document analysis and recognition (ICDAR), Vol. 1, IEEE, 2017, pp. 708–713.
- [23] Q. N. Vo, S. H. Kim, H. J. Yang, G. Lee, Binarization of degraded document images based on hierarchical deep supervised network, *Pattern Recognition* 74 (2018) 568–586.
- [24] S. He, L. Schomaker, Deepotsu: Document enhancement and binarization using iterative deep learning, *Pattern recognition* 91 (2019) 379–390.
- [25] I. Goodfellow, J. Pouget-Abadie, M. Mirza, B. Xu, D. Warde-Farley, S. Ozair, A. Courville, Y. Bengio, Generative adversarial networks, *Communications of the ACM* 63 (11) (2020) 139–144.
- [26] P. Isola, J.-Y. Zhu, T. Zhou, A. A. Efros, Image-to-image translation with conditional adversarial networks, in: Proceedings of the IEEE conference on computer vision and pattern recognition, 2017, pp. 1125–1134.
- [27] M. Mirza, S. Osindero, Conditional generative adversarial nets, arXiv preprint arXiv:1411.1784 (2014).
- [28] A. K. Bhunia, A. K. Bhunia, A. Sain, P. P. Roy, Improving document binarization via adversarial noise-texture augmentation, in: 2019 IEEE International Conference on Image Processing (ICIP), IEEE, 2019, pp. 2721–2725.
- [29] J. Zhao, C. Shi, F. Jia, Y. Wang, B. Xiao, Document image binarization with cascaded generators of conditional generative adversarial networks, *Pattern Recognition* 96 (2019) 106968.
- [30] R. De, A. Chakraborty, R. Sarkar, Document image binarization using dual discriminator generative adversarial networks, *IEEE Signal Processing Letters* 27 (2020) 1090–1094.
- [31] S. Suh, J. Kim, P. Lukowicz, Y. O. Lee, Two-stage generative adversarial networks for binarization of color document images, *Pattern Recognition* 130 (2022) 108810.
- [32] R. Keys, Cubic convolution interpolation for digital image processing, *IEEE transactions on acoustics, speech, and signal processing* 29 (6) (1981) 1153–1160.
- [33] A. Haar, Zur theorie der orthogonalen funktionensysteme, *Mathematische Annalen* 69 (1910) 331–371.
- [34] Z. Zhou, M. M. Rahman Siddiquee, N. Tajbakhsh, J. Liang, Unet++: A nested u-net architecture for medical image segmentation, in: Deep Learning in Medical Image Analysis and Multimodal Learning for Clinical Decision Support: 4th International Workshop, DLMIA 2018, and 8th International Workshop, ML-CDS 2018, Held in Conjunction with MICCAI 2018, Granada, Spain, September 20, 2018, Proceedings 4, Springer, 2018, pp. 3–11.
- [35] Z. Zhou, M. M. R. Siddiquee, N. Tajbakhsh, J. Liang, Unet++: Redesigning skip connections to exploit multiscale features in image segmentation, *IEEE transactions on medical imaging* 39 (6) (2019) 1856–1867.
- [36] M. Tan, Q. Le, Efficientnet: Rethinking model scaling for convolutional neural networks, in: International conference on machine learning, PMLR, 2019, pp. 6105–6114.
- [37] I. Gulrajani, F. Ahmed, M. Arjovsky, V. Dumoulin, A. C. Courville, Improved training of wasserstein gans, *Advances in neural information processing systems* 30 (2017).
- [38] E. R. Bartusiak, S. K. Yarlagadda, D. Güera, P. Bestagini, S. Tubaro, F. M. Zhu, E. J. Delp, Splicing detection and localization in satellite imagery using conditional gans, in: 2019 IEEE Conference on Multimedia Information Processing and Retrieval (MIPR), IEEE, 2019, pp. 91–96.
- [39] C. Li, M. Wand, Precomputed real-time texture synthesis with markovian generative adversarial networks, in: European conference on computer vision, Springer, 2016, pp. 702–716.
- [40] J.-Y. Zhu, T. Park, P. Isola, A. A. Efros, Unpaired image-to-image translation using cycle-consistent adversarial networks, in: Proceedings of the IEEE international conference on computer vision, 2017, pp. 2223–2232.
- [41] C. Ledig, L. Theis, F. Huszár, J. Caballero, A. Cunningham, A. Acosta, A. Aitken, A. Tejani, J. Totz, Z. Wang, et al., Photo-realistic single image super-resolution using a generative adversarial network, in: Proceedings of the IEEE conference on computer vision and pattern recognition, 2017, pp. 4681–4690.
- [42] B. Gatos, K. Ntirogiannis, I. Pratikakis, Icdar 2009 document image binarization contest (dibco 2009), in: 2009 10th International conference on document analysis and recognition, IEEE, 2009, pp. 1375–1382.
- [43] I. Pratikakis, B. Gatos, K. Ntirogiannis, H-dibco 2010-handwritten document image binarization competition, in: 2010 12th International Conference on Frontiers in Handwriting Recognition, IEEE, 2010, pp. 727–732.
- [44] I. Pratikakis, B. Gatos, K. Ntirogiannis, Icfhr 2012 competition on handwritten document image binarization (h-dibco 2012), in: 2012 international conference on frontiers in handwriting recognition, IEEE, 2012, pp. 817–822.
- [45] S. M. Ayatollahi, H. Z. Nafchi, Persian heritage image binarization competition (phibc 2012), in: 2013 First Iranian Conference on Pattern Recognition and Image Analysis (PRIA), IEEE, 2013, pp. 1–4.
- [46] F. Deng, Z. Wu, Z. Lu, M. S. Brown, Binarizationshop: a user-assisted software suite for converting old documents to black-and-white, in: Proceedings of the 10th annual joint conference on Digital libraries, 2010, pp. 255–258.
- [47] S. K. Jemni, M. A. Souibgui, Y. Kessentini, A. Fornés, Enhance to read better: a multi-task adversarial network for handwritten document image enhancement, *Pattern Recognition* 123 (2022) 108370.
- [48] Z. Yang, B. Liu, Y. Xiong, G. Wu, Gdb: gated convolutions-based document binarization, *Pattern Recognition* 146 (2024) 109989.
- [49] D. Kingma, J. Ba, Adam: A method for stochastic optimization, in: International Conference on Learning Representations (ICLR), 2015.
- [50] J. Deng, W. Dong, R. Socher, L.-J. Li, K. Li, L. Fei-Fei, Imagenet: A large-scale hierarchical image database, in: 2009 IEEE conference on computer vision and pattern recognition, IEEE, 2009, pp. 248–255.
- [51] R.-Y. Ju, Y.-S. Lin, J.-S. Chiang, C.-C. Chen, W.-H. Chen, C.-T. Chien, Ccdwt-gan: Generative adversarial networks based on color channel using discrete wavelet transform for document image binarization, in: 20th Pacific Rim International Conference on Artificial Intelligence, PRICAI 2023, Jakarta, Indonesia, November 15–19, Springer Nature Singapore, 2023, pp. 186–198.
- [52] R. S. Stanković, B. J. Falkowski, The haar wavelet transform: its status and achievements, *Computers & Electrical Engineering* 29 (1) (2003) 25–44.

CRediT authorship contribution statement

Rui-Yang Ju : Conceptualization, Methodology, Writing – original draft. **Yu-Shian Lin** : Methodology, Data curation, Investigation. **Yanlin Jin** : Software, Validation, Writing – review & editing. **Chih-Chia Chen** : Formal Analysis, Project administration. **Chun-Tse Chien** : Visualization. **Jen-Shiun Chiang** : Funding acquisition, Supervision, Writing – review & editing.